


Article

Styles of Alteration of Ti Oxides of the Kimberlite Groundmass: Implications on the Petrogenesis and Classification of Kimberlites and Similar Rocks

Jingyao Xu ^{1,*} , Joan Carles Melgarejo ¹  and Montgarri Castillo-Oliver ²

¹ Department of Mineralogy, Petrology and Applied Geology, Faculty of Earth Sciences, University of Barcelona, 08028 Barcelona, Spain; joan.carles.melgarejo.draper@ub.edu

² ARC Centre of Excellence for Core to Crust Fluid Systems and GEMOC, Department of Earth and Planetary Sciences, Macquarie University, Sydney, NSW 2019, Australia; montgarri.castillo-oliver@mq.edu.au

* Correspondence: jingyao.xu@ub.edu; Tel.: +34-934-020-406

Received: 27 November 2017; Accepted: 1 February 2018; Published: 6 February 2018

Abstract: The sequence of replacement in groundmass perovskite and spinel from SK-1 and SK-2 kimberlites (Eastern Dharwar craton, India) has been established. Two types of perovskite occur in the studied Indian kimberlites. Type 1 perovskite is found in the groundmass, crystallized directly from the kimberlite magma, it is light rare-earth elements (LREE)-rich and Fe-poor and its ΔNNO calculated value is from -3.82 to -0.73 . The second generation of perovskite (type 2 perovskite) is found replacing groundmass atoll spinel, it was formed from hydrothermal fluids, it is LREE-free and Fe-rich and has very high ΔNNO value (from 1.03 to 10.52). Type 1 groundmass perovskite may be either replaced by anatase or kassite along with aeschynite-(Ce). These differences in the alteration are related to different $f(\text{CO}_2)$ and $f(\text{H}_2\text{O})$ conditions. Furthermore, primary perovskite may be strongly altered to secondary minerals, resulting in redistribution of rare-earth elements (REE) and, potentially, U, Pb and Th. Therefore, accurate petrographic and chemical analyses are necessary in order to demonstrate that perovskite is magmatic before proceeding to sort geochronological data by using perovskite. Ti-rich hydrogarnets (12.9 wt %–26.3 wt % TiO_2) were produced during spinel replacement by late hydrothermal processes. Therefore, attention must be paid to the position of Ca-Ti-garnets in the mineral sequence and their water content before using them to classify the rock based on their occurrence.

Keywords: perovskite alteration; Ti-rich garnet; aeschynite-(Ce); kassite; anatase; hydrothermal perovskite

1. Introduction

Ti-rich minerals from kimberlite such as ilmenite, spinels, rutile and perovskite are important carriers of petrogenetic information. Xenocrystic Ti-rich oxides in kimberlitic rock, such as Cr-rich rutile, Ti-rich spinel and ilmenite, provide information about the metasomatic processes in the cratonic lithospheric mantle [1,2]. In addition, Ti-rich oxides from kimberlite groundmass, such as Ti-rich spinel [3] and perovskite [4], could supply information about the evolution of kimberlitic magmas. Finally, perovskite [5,6] and rutile [7,8] could also be used to determine the kimberlite emplacement age. However, in many cases these minerals undergo complex alteration processes during the hydrothermal or supergene late stages of the kimberlite crystallization sequence that could disturb the petrogenetic interpretations based on geochemical data.

Perovskite is a principal host of LREE in SiO_2 -undersaturated ultramafic and alkaline rocks [9] and is a mineral that may be produced along different crystallization stages of these magmas.

Therefore, the chemical and textural study of these generations can provide information about several stages of magmatic crystallization [10,11]. The crystallization of magmatic perovskite is produced later than that of macrocrystal spinel; and simultaneously with “reaction” Fe-rich spinel and groundmass spinels of the magnesian ulvöspinel—magnetite series in kimberlite [12].

However, perovskite may be unstable in CO₂-rich fluid environments characteristic of the final stage of some carbonatites and kimberlites worldwide [12–14]. Products of perovskite replacement in kimberlites may include kassite, anatase and titanite along with calcite, ilmenite and unidentified LREE-Ti oxides [13,15]. Similarly, carbonatitic perovskite is replaced by anatase with calcite and finally by ilmenite and ancylite [13]. In consequence, only pristine unaltered perovskite has been used to establish U-Pb age [16–18] and Sr-Nd-Pb isotopic composition [19–21] from different worldwide kimberlites.

However, perovskite cannot be formed only by magmatic processes. A metasomatic origin has been inferred for perovskite from carbonatites [22,23] and perovskite from skarns is also widely described as a hydrothermal product [9].

Primary Ti-rich garnet is considered as a key mineral for the classification of ultramafic lamprophyres, such as aillikites [24] and orangeites [25]. Ti-rich garnets classified as andradite, schorlomite, zirconian schorlomite and kimzeyite occur in the Torngat aillikite dykes [24]; kimzeyite and Ti-andradite from Aillik Bay are considered as primary magmatic minerals and are indicators of the aillikitic affinity of these rocks [26]. A primary magmatic origin has also been suggested for the Ca-Ti-Fe rich garnets found in orangeite from Swartruggens [27]. However, Ti-rich hydrogarnets can be produced by subsolidus reactions in a wide span of environments, as in metapyroxenites [28], serpentinites [29], basalts from the oceanic seafloor [30] and magmatic alkaline rocks and carbonatites [31].

Therefore, the Ti-rich minerals can supply information of petrological or economic interest. However, these minerals can be easily altered by subsolidus processes. In addition, the hydrothermal occurrences of these minerals in other geological environments suggest that these minerals can be produced by the reaction of the existing magmatic minerals with late hydrothermal or supergene fluids. In the present work, we describe the different alteration styles of groundmass Ti-rich oxide (perovskite and spinel) from SK-1 and SK-2 kimberlites (Eastern Dharwar craton, India), including the neoformation of pristine perovskite and Ti-rich hydrogarnets by subsolidus processes. The petrogenetic implications are discussed.

2. Geological Setting

Kimberlites occur in the Bastar craton (central India) and the Eastern Dharwar craton (EDC, southern India) in India. Kimberlite intrusions (around 100 bodies) found in the EDC of southern India are distributed in three fields: (1) the southern Wajrakarur kimberlite field; (2) the northern Narayanpet kimberlite field; and (3) the Raichur kimberlite field (RKF) [17,32]. This work studied two sequences of alteration in samples from two nearby pipes (SK-1 and SK-2, about 1100 m of distance) from Siddanpalli, RKF, EDC, southern India (Figure 1). Emplacement of these two kimberlites took place during the Mesoproterozoic around 1.1 Ga [17].

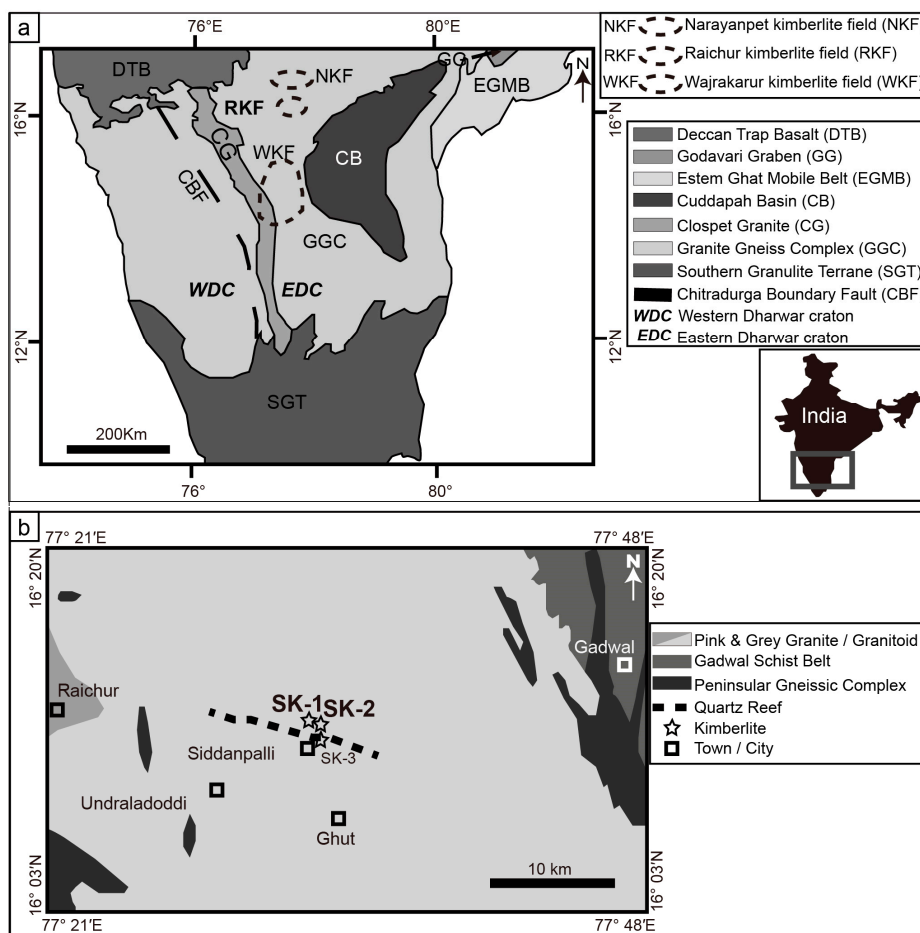


Figure 1. (a) Simplified geological map of Southern India showing locations of Narayanpet kimberlite field (NKF), Raichur kimberlite field (RKF) and Wajrakarur kimberlite field (WKF), adapted from Dongre [32]; (b) Geological setting of the Siddanpalli kimberlites in the RKF, showing the studied kimberlite samples, adapted from Chalapathi Rao et al. [17].

3. Methods

Minerals have been identified in situ on thin polished section by SEM-BSE-EDS, EMPA and Raman spectroscopy at the Scientific and Technological Centers of the University of Barcelona (CCiTUB), Barcelona, Spain.

Petrographic and textural studies were carried out using optical and scanning electron microscopy (SEM), the latter employing an E-SEM-Quanta 200 FEI-XTE-325/D8395 (FEI, Hillsboro, OR, USA) with a BSE detector and coupled to a Genesis EDS microanalysis system. The operating conditions were 20–25 kV, 1 nA beam current and 10 mm distance to detector.

The compositional study was carried out using an electron microprobe (EMPA) JEOL JXA-8230 (JEOL, Tokyo, Japan), equipped with five wavelength dispersive spectrometers (WDS) and an energy dispersive spectrometer (EDS), at the CCiTUB. The operating conditions were: accelerating voltage of 20 kV combined with a beam current 15 nA. Calibration standards and analytical crystals used for the analyses of perovskite and kassite were: wollastonite (Si, TAP, $K\alpha$), corundum (Al, TAP, $K\alpha$), rutile (Ti, PETJ, $K\alpha$), CeO_2 (Ce, PETJ, $L\alpha$), LaB_6 (La, PETJ, $L\alpha$), periclase (Mg, TAPH, $K\alpha$), albite (Na, TAPH, $K\alpha$), Ta (Ta, LIFH, $L\alpha$), Fe_2O_3 (Fe, LIFH, $K\alpha$), rhodonite (Mn, LIFH, $K\alpha$), REE-1 (Pr, LIFH, $L\beta$), REE-4 (Nd, LIFH, $L\alpha$), barite (Ba, LIFH, $L\alpha$), wollastonite (Ca, PETL, $K\alpha$), orthoclase (K_2O , PETL, $K\alpha$), Nb (Nb, PETL, $L\alpha$), $ZrSiO_4$ (Zr, PETL, $L\alpha$), celestine (Sr, PETL, $L\alpha$).

Calibration standards and analytical crystals used for the analyses of aeschynite were the following: celestine (Sr, PETJ, $L\alpha$), YAG (Y_2O_3 , PETJ, $L\alpha$), ZrO_2 (Zr, PETJ, $L\alpha$), Nb (Nb, PETJ, $L\alpha$), wollastonite (Ca, PETJ, $K\alpha$), UO_2 (U, PETJ, Mb), ThO_2 (Th, PETJ, $M\alpha$), albite (Na, TAPH, $K\alpha$), periclase (Mg, TAPH, $K\alpha$), corundum (Al, TAPH, $K\alpha$), wollastonite (Si, TAPH, $K\alpha$), fluorite (F, TAPH, $K\alpha$), barite (Ba, LIFH, $L\alpha$), rutile (Ti, LIFH, $K\alpha$), LaB_6 (La, LIFH, $L\alpha$), CeO_2 (Ce, LIFH, $L\alpha$), REE-4 (Nd, LIFH, Lb), Cr_2O_3 (Cr, LIFH, $K\alpha$), REE-1 (Pr, LIFH, Lb), rhodonite (Mn, LIFH, $K\alpha$), REE-3 (Sm, LIFL, Lb), Fe_2O_3 (Fe, LIFL, $K\alpha$), REE-3 (Gd, LIFL, Lb), REE-1 (Er, LIFL, $L\alpha$), REE-1 (Dy, LIFL, Lb), Hf (Hf, LIFL, $L\alpha$), Ta (Ta, LIFL, $L\alpha$), PbS (Pb, LIFL, $L\alpha$).

Calibration standards and analytical crystals used for the analyses of Ti-rich garnets were: wollastonite (Si, TAP, $K\alpha$), corundum (Al, TAP, $K\alpha$), Cr_2O_3 (Cr, PETJ, $K\alpha$), rutile (Ti, PETJ, $K\alpha$), periclase (Mg, TAPH, $K\alpha$), albite (Na, TAPH, $K\alpha$), barite (Ba, LIFH, $L\alpha$), rhodonite (Mn, LIFH, $K\alpha$), Fe_2O_3 (Fe, LIFH, $K\alpha$), celestine (Sr, PETL, $L\alpha$), $ZrSiO_4$ (Zr, PETL, $L\alpha$), orthoclase (K_2O , PETL, $K\alpha$), wollastonite (Ca, PETL, $K\alpha$).

Micro Raman analyses were obtained at the CCiTUB by using a HORIBA Jobin Yvon LabRam HR 800 dispersive spectrometer (HORIBA, Kyoto, Japan), equipped with an Olympus BXFM optical microscope. Non-polarized Raman spectra were obtained by applying a 532 nm laser, the pixel size was 1 μm . The exposure time was 5 s with 3 scans and laser power at sample was 2.5 mW for anatase. The exposure time was 5 s with 10 scans and laser power at sample was 5 mW for kassite. The exposure time was 20 s with 5 scans and laser power at sample was 1.25 mW for garnet.

4. Results

4.1. Mineral Textures

Both kimberlites have similar xenocrysts, mainly consisting of Ti oxides such as rutile and ilmenite, scattered in a fine-grained groundmass. Primary groundmass minerals are also similar in both kimberlites and the dominant minerals include calcite, apatite, perovskite and altered atoll-shaped spinel-group minerals. The abundance of minerals of the serpentine group in the groundmass suggests that olivine was also common in these kimberlites.

Groundmass perovskite (type 1 perovskite) from SK-1 is euhedral, zoned and slightly replaced by anatase following grain borders and small cracks (Figure 2a). Ti-rich spinel-group minerals in groundmass are strongly altered to serpentine, calcite, magnetite and cryptocrystalline Ti-rich andradite (Figure 2b,c).

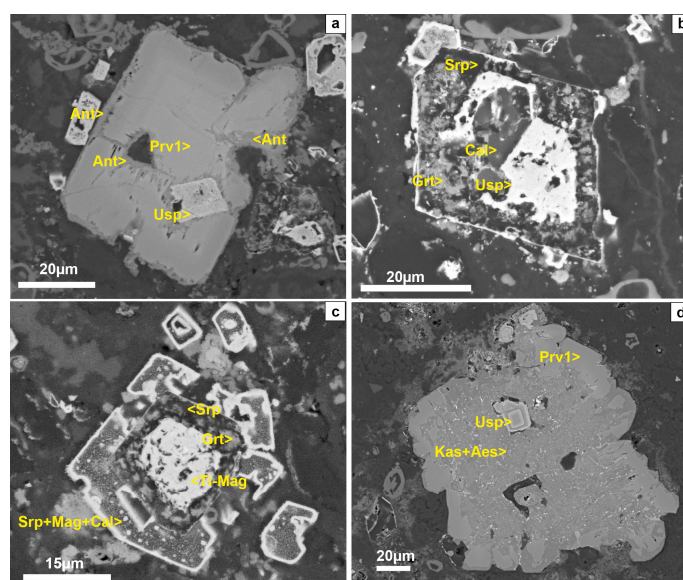


Figure 2. Cont.

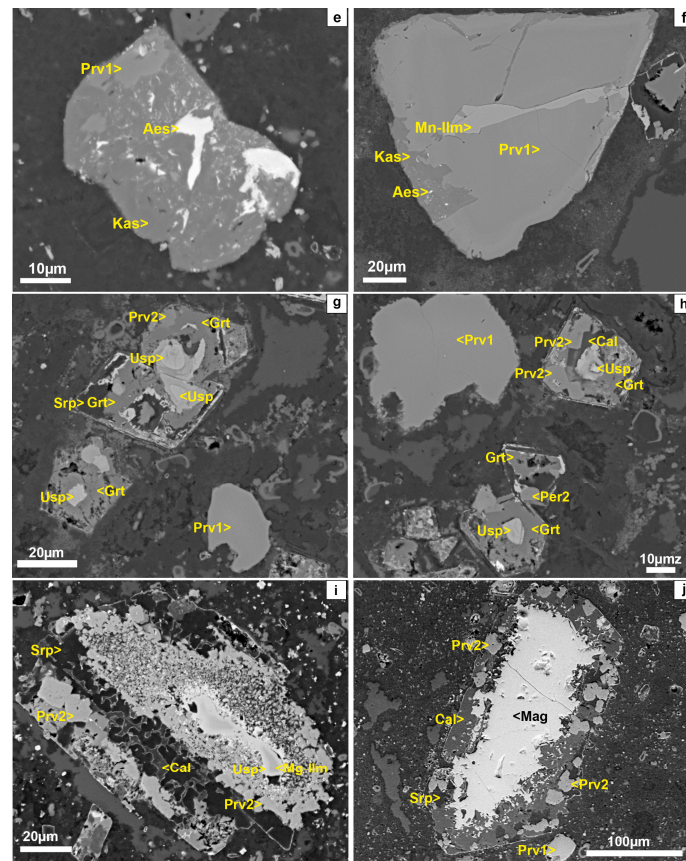


Figure 2. Representative SEM (BSE) images of the groundmass from SK-1 and SK-2 kimberlites. (a) Type 1 perovskite (Prv1) with an ulvöspinel inclusion (Usp) from SK-1 kimberlites being replaced by anatase (Ant) along borders and fractures; (b) Euhedral atoll spinel from SK-1, replaced by serpentine (Srp), calcite (Cal) and cryptocrystalline Ti-rich garnets (Grt), with a relict of ulvöspinel (Usp) in the centre of the crystal; (c) Atoll spinel from SK-1, altered to serpentine, calcite, magnetite (Mag) and cryptocrystalline Ti-rich garnets, with a relict of titanomagnetite (Ti-Mag) in the centre; (d) Type 1 groundmass perovskite from SK-2 kimberlite, replaced by kassite (Kas) with aeschynite (Aes); (e) Type 1 groundmass perovskite from SK-2, replaced by kassite with aeschynite; (f) Type 1 perovskite from SK-2, altered to kassite and aeschynite (Kas + Aes) in grain borders; the ensemble is replaced by Mn-rich ilmenite (Mn-ilm) along fractures and grain borders; (g) Groundmass atoll spinel from SK-2 altered to type 2 perovskite (Prv2), Ti-rich garnets and serpentine, showing ulvöspinel relicts; (h) Atoll groundmass spinel from SK-2 altered to type 2 euhedral perovskite, Ti-rich garnets and calcite, showing relicts of ulvöspinel and type 1 perovskite; (i) Mg-rich ilmenite (Mg-ilm) from SK-2, replaced by ulvöspinel, which on its turn is replaced by type 2 perovskite, calcite and serpentine; (j) Magnetite from SK-2, replaced by type 2 euhedral perovskite, serpentine and calcite.

Groundmass perovskite (type 1 perovskite) from SK-2 is euhedral to subhedral and it has oscillatory zoning. This perovskite is partially or nearly totally replaced by kassite $[\text{CaTi}_2\text{O}_4(\text{OH})_2]$ accompanied by abundant aeschynite-(Ce), ideally $[(\text{Ce},\text{Ca},\text{Fe},\text{Th})(\text{Ti},\text{Nb})_2(\text{O},\text{OH})_6]$ (Figure 2d–f). The ensemble may also be replaced by Mn-rich ilmenite along small cracks (Figure 2f). In addition, a second perovskite generation (type 2 perovskite, euhedral) replaces the groundmass atoll spinel along with Ti-rich hydrogarnets, calcite and serpentine (Figure 2g,h). Type 2 perovskite often shows a geode-like texture into the pseudomorphized atoll spinel (Figure 2h). Ilmenite and magnetite xenocrysts from SK-2 may also be replaced by a sequence of typical groundmass minerals and sometimes by type 2 perovskite (Figure 2i,j); on its turn, this type 2 perovskite may be replaced by anatase.

4.2. MicroRaman Study

Identity of anatase was confirmed by microRaman spectroscopy and its spectrum was compared with that of submicroscopic anatase, mixed with calcite, altering perovskite in carbonatites [14,15] (Figure 3a). Calcite has a peak at 1088 cm^{-1} which corresponds to the vibration of the CO_3 group [15]. However, calcite is absent from the products of alteration of the perovskite from Siddanpalli.

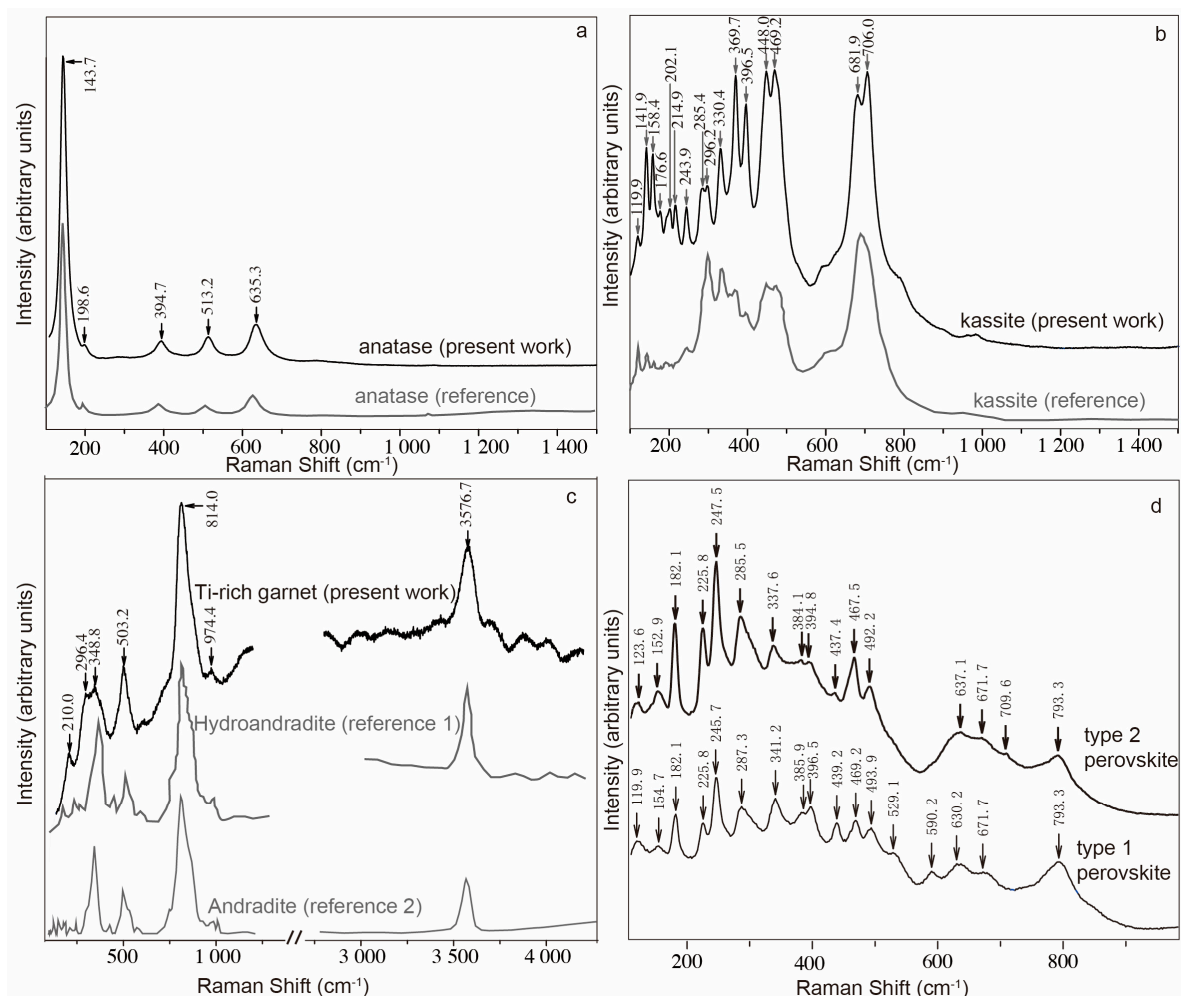


Figure 3. Representative Raman spectrum analysed in: (a) anatase from SK-1 kimberlite (present work) compared with anatase reference from Martins et al. [15], the last presents a peak at 1088 cm^{-1} which corresponds to calcite; (b) kassite from SK-2 kimberlite (present work) compared with kassite from Martins et al. [15]; (c) Ti-rich garnet from SK-2 kimberlite, compared with grossular-hydroandradite from Ghosh et al. [33] and andradite from the RRUFF Project database (R060350) [34]; (d) type 2 perovskite replacing spinel and type 1 groundmass perovskite from SK-2 (present work).

Kassite [$\text{CaTi}_2\text{O}_4(\text{OH})_2$] has a very similar chemical composition to cafetite ($\text{CaTi}_2\text{O}_5 \cdot \text{H}_2\text{O}$). The identification of kassite from the SK-2 kimberlite was confirmed by comparing the kassite Raman spectrum with the available spectrum of kassite standards [15] (Figure 3b).

Raman spectra of Ti-rich garnet from SK-2 kimberlite is also recorded (Figure 3c) and shows a peak at 3576 cm^{-1} which corresponds to the OH vibration [30]. The spectrum was compared with those of other hydrogarnets [33,34].

The microRaman study also confirmed the identification of the second generation of perovskite (type 2) by comparison with the spectrum of the magmatic perovskite (type 1) (Figure 3d). Minor differences in

the position and intensity of the bands can also be related to changes in the chemical composition or to different orientation.

Finally, the Raman analysis was helpful to establish the identity of aeschynite-(Ce). In this case, most of the bands have similarities with those from the published standards of members of the aeschynite group. Minor differences in the positions of the bands can be explained because the studied aeschynite is Ta-poor and La- and Nd-rich when compared with the standard aeschynites [35,36].

4.3. Mineral Chemistry

Spinel-group minerals from groundmass of both kimberlites have compositions in the ulvöspinel-titanomagnetite domain. However, they are strongly altered and the relict cores may be seldom enriched in Zn (0.1 wt %–2.0 wt % ZnO in SK-1 and 0 wt %–7.5 wt % ZnO in SK-2).

Compositional trends of type 1 groundmass perovskite are similar for both kimberlites (Table 1, Figure 4). Hence, the cores of the perovskite crystals from SK-1 are slightly enriched in REE (4.9 wt %–8.4 wt % Σ LREE₂O₃), whereas their rims have only 1.9 wt %–3.7 wt % Σ LREE₂O₃; similarly, perovskite crystals from SK-2 have 4.0 wt %–5.5 wt % Σ LREE₂O₃ in the centres and 0.9 wt %–2.6 wt % Σ LREE₂O₃ in the borders. Nb is also slightly enriched in the cores compared to the rims (0.6 wt %–1.1 wt % Nb₂O₅ in the cores and 0.4 wt %–0.6 wt % Nb₂O₅ in the rims in SK-1; 0.5 wt %–0.8 wt % Nb₂O₅ in the cores and 0.4 wt %–0.6 wt % Nb₂O₅ in the rims in SK-2). Type 1 perovskite in both kimberlites has Fe₂O₃ contents ranging 1.0 wt %–1.7 wt % (Table 1, Figure 4).

Type 2 perovskite from the SK-2 kimberlite has different composition than type 1 perovskite. It is depleted in LREE (<1 wt % Σ LREE₂O₃) and Nb (<0.1 wt % Nb₂O₅) but it has higher Fe contents (2.0 wt %–4.0 wt % Fe₂O₃) than type 1 perovskite (Figure 4, Table 1).

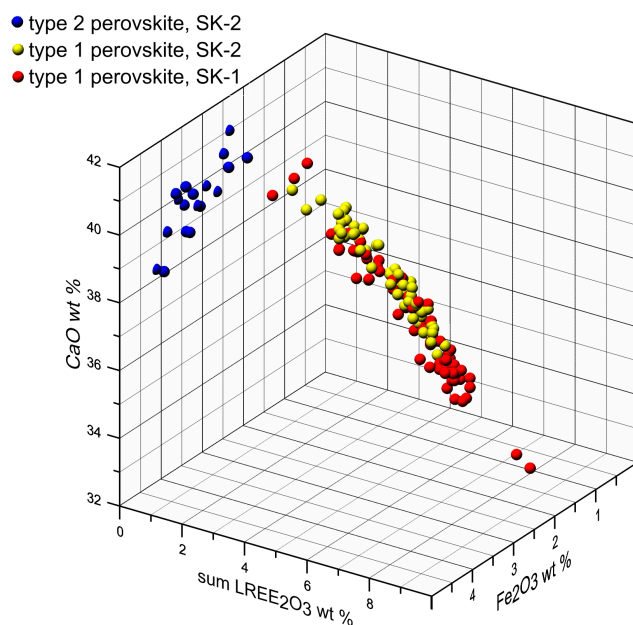


Figure 4. CaO- Σ LREE₂O₃-Fe₂O₃ (wt %) plot of type 1 perovskite from SK-1 and SK-2 and type 2 perovskite from SK-2.

Table 1. Representative electron microprobe (EMPA) analysis of type 1 perovskite from SK-1 and SK-2 kimberlites, type 2 perovskite, aeschynite-(Ce) and kassite from SK-2 kimberlite.

Mineral	Type 1 Perovskite								Type 2 Perovskite		Aeschynite-(Ce)		Kassite		
	SK-1				SK-2				SK-2	SK-2	SK-2	SK-2	SK-2	SK-2	
	(wt %)	Centre	Centre	Border	Border	Centre	Centre	Border							Border
SrO	0.34	0.18	0.23	0.25	0.20	0.19	0.20	0.24	bdl	bdl	0.13	bdl	bdl	bdl	bdl
ZrO ₂	0.10	0.21	0.23	0.38	0.08	0.14	0.19	0.28	0.09	0.46	0.74	0.25	0.43	0.40	0.08
Nb ₂ O ₅	0.60	0.98	0.73	0.61	0.54	0.63	0.44	0.50	0.10	bdl	3.10	0.99	0.63	0.46	0.62
CaO	34.68	34.64	37.11	37.63	35.36	35.27	38.06	38.19	39.95	38.20	7.24	8.00	22.49	22.12	21.32
ThO ₂	-	-	-	-	-	-	-	-	-	-	0.37	bdl	-	-	-
Na ₂ O	0.57	0.57	0.35	0.22	36.53	0.60	0.28	0.22	bdl	bdl	bdl	bdl	bdl	bdl	bdl
MgO	0.06	bdl	0.05	0.09	0.08	bdl	0.05	0.05	0.14	0.08	0.04	0.05	0.26	0.05	bdl
Al ₂ O ₃	0.33	0.30	0.24	0.31	0.25	0.29	0.23	0.28	bdl	bdl	bdl	bdl	bdl	0.03	bdl
SiO ₂	bdl	bdl	bdl	0.04	bdl	bdl	bdl	bdl	0.61	0.60	0.38	bdl	0.05	0.06	0.07
BaO	0.19	0.12	-	0.08	-	0.13	0.18	0.12	-	-	0.46	0.15	-	-	-
TiO ₂	54.36	54.26	54.13	56.30	54.99	54.75	57.10	56.67	55.49	53.48	48.61	52.20	62.42	64.74	65.26
La ₂ O ₃	0.97	1.02	0.67	0.50	0.60	0.84	0.62	0.53	bdl	bdl	7.79	11.11	bdl	bdl	0.15
Ce ₂ O ₃	3.07	3.03	1.79	0.88	2.18	2.84	0.89	0.89	bdl	bdl	18.34	17.99	0.23	0.48	0.58
Nd ₂ O ₃	1.56	1.50	1.08	0.35	1.18	1.50	0.34	0.41	bdl	bdl	6.88	3.99	0.24	0.22	0.28
Cr ₂ O ₃	-	-	-	-	-	-	-	-	-	-	bdl	0.05	-	-	-
Pr ₂ O ₃	0.45	0.43	0.17	0.19	0.08	0.36	0.19	0.17	bdl	bdl	1.97	1.45	0.12	0.08	bdl
MnO	0.02	0.05	0.04	bdl	0.03	bdl	0.02	0.05	bdl	0.03	bdl	0.19	0.15	0.37	1.28
Sm ₂ O ₃	-	-	-	-	-	-	-	-	-	-	0.51	0.19	-	-	-
Fe ₂ O ₃	1.28	1.36	1.74	1.31	0.99	1.29	1.16	1.01	2.00	4.03	0.59	0.66	1.29	0.93	0.51
Gd ₂ O ₃	-	-	-	-	-	-	-	-	-	-	0.24	0.13	-	-	-
HfO ₂	-	-	-	-	-	-	-	-	-	-	0.11	bdl	-	-	-
Ta ₂ O ₅	bdl	bdl	bdl	bdl	bdl	bdl	bdl	bdl	0.07	bdl	0.06	0.11	bdl	0.04	bdl
K ₂ O	0.04	0.03	0.02	0.00	0.03	0.03	0.02	0.02	0.00	0.02	-	-	bdl	0.01	bdl
Total	98.63	98.74	98.57	99.16	98.25	98.92	99.99	99.65	98.80	97.19	97.53	97.79	88.37	90.05	90.19
ΣLREE ₂ O ₃	6.04	5.98	3.70	1.93	4.04	5.54	2.04	1.99	0.14	0.15	35.49	34.73	0.59	0.81	1.03

Table 1. Cont.

Mineral	Type 1 Perovskite								Type 2 Perovskite		Aeschynite-(Ce)		Kassite		
	SK-1				SK-2				SK-2	SK-2	SK-2	SK-2	SK-2	SK-2	SK-2
	(wt %)	Centre	Centre	Border	Border	Centre	Centre	Border							
(apfu)	O = 3								O = 3		Σcations = 3		Σcations = 3		
Sr	0.005	0.003	0.003	0.003	0.003	0.003	0.003	0.003	0.000	0.000	0.004	0.000	0.000	0.000	0.000
Y	-	-	-	-	-	-	-	-	-	-	0.000	0.000	-	-	-
Zr	0.001	0.002	0.003	0.004	0.001	0.002	0.002	0.003	0.001	0.005	0.018	0.006	0.001	0.001	0.001
Nb	0.006	0.011	0.008	0.006	0.006	0.007	0.005	0.005	0.001	0.000	0.070	0.022	0.012	0.008	0.011
Ca	0.885	0.883	0.938	0.932	0.924	0.894	0.936	0.942	0.985	0.960	0.387	0.417	0.986	0.957	0.926
Th	-	-	-	-	-	-	-	-	-	-	0.004	0.000	-	-	-
Na	0.026	0.026	0.016	0.010	0.022	0.027	0.012	0.010	0.000	0.001	0.000	0.000	0.000	0.000	0.000
Mg	0.002	0.001	0.002	0.003	0.003	0.000	0.002	0.002	0.005	0.003	0.003	0.004	0.016	0.003	0.000
Al	0.009	0.008	0.007	0.008	0.007	0.008	0.006	0.008	0.000	0.000	0.000	0.000	0.000	0.001	0.000
Si	0.000	0.000	0.000	0.001	0.000	0.000	0.000	0.000	0.014	0.014	0.019	0.000	0.002	0.002	0.003
Ba	0.002	0.001	0.000	0.001	0.000	0.001	0.002	0.001	-	-	0.009	0.003	-	-	-
Ti	0.974	0.970	0.960	0.979	0.977	0.974	0.985	0.981	0.960	0.943	1.823	1.908	1.922	1.967	1.990
La	0.008	0.008	0.005	0.004	0.005	0.007	0.005	0.004	0.000	0.000	0.132	0.184	0.000	0.000	0.002
Ce	0.027	0.026	0.015	0.007	0.019	0.025	0.007	0.007	0.000	0.000	0.335	0.320	0.004	0.007	0.009
Nd	0.013	0.013	0.009	0.003	0.010	0.013	0.003	0.003	0.000	0.000	0.123	0.069	0.003	0.003	0.004
Cr	-	-	-	-	-	-	-	-	-	-	0.000	0.002	-	-	-
Pr	0.004	0.004	0.001	0.002	0.001	0.003	0.002	0.001	0.000	0.000	0.036	0.026	0.002	0.001	0.000
Mn	0.000	0.001	0.001	0.000	0.000	0.000	0.000	0.001	0.000	0.000	0.000	0.006	0.004	0.010	0.036
Sm	-	-	-	-	-	-	-	-	-	-	0.009	0.003	-	-	-
Fe	0.023	0.024	0.031	0.023	0.018	0.023	0.020	0.017	0.035	0.071	0.022	0.024	0.040	0.028	0.016
Gd	-	-	-	-	-	-	-	-	-	-	0.004	0.002	-	-	-
Hf	-	-	-	-	-	-	-	-	-	-	0.002	0.000	-	-	-
Ta	0.000	0.000	0.000	0.000	0.000	0.000	0.000	0.000	0.000	0.000	0.001	0.001	0.000	0.000	0.000
K	0.001	0.001	0.001	0.000	0.001	0.001	0.001	0.001	0.000	0.000	-	-	0.000	0.000	0.000
ΣLREE	0.052	0.051	0.031	0.016	0.034	0.047	0.017	0.016	0.001	0.001	0.512	0.533	0.009	0.012	0.015

“bdl”: below detection limit; “-”: not analysed.

Frequency histograms of $\log fO_2$ expressed relative to the NNO buffer (ΔNNO) calculated using the perovskite oxybarometer developed by Bellis and Canil [4] are shown in Figure 5. Type 1 perovskite in SK-1 and SK-2 has similar ΔNNO value (from -0.73 to -3.40 in SK-1 and from -1.07 to -3.82 in SK-2) but type 2 perovskite has very high ΔNNO value (from 1.03 to 10.52) and was formed in a highly oxidizing environment.

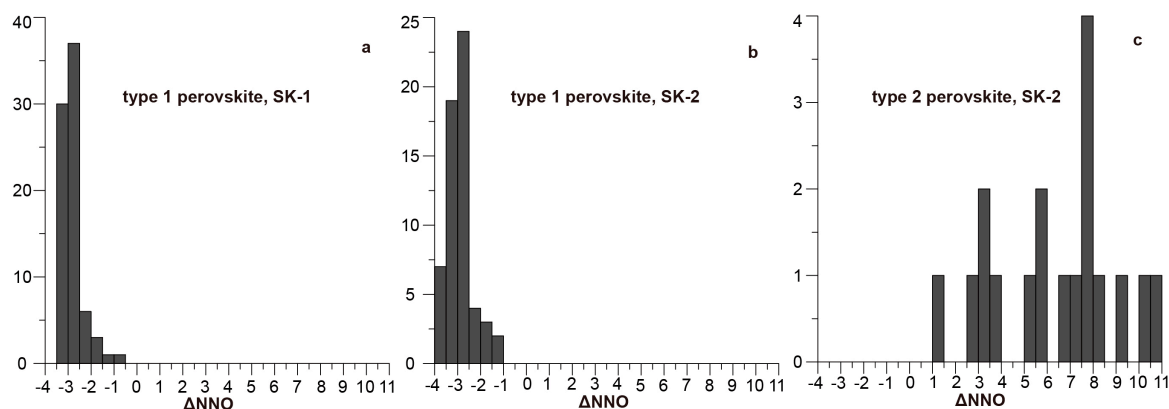


Figure 5. Frequency histograms of $\log fO_2$ expressed relative to the NNO buffer (ΔNNO) calculated using the perovskite oxybarometer developed by Bellis and Canil [4]. (a) type 1 perovskite from SK-1; (b) type 1 perovskite from SK-2; (c) type 2 perovskite from SK-2.

Kassite replacing type 1 perovskite in SK-2 has a stoichiometric composition (Table 1), whereas the associated aeschynite-(Ce) tends to concentrate LREE and, to a lesser extent, Nb. The aeschynite-(Ce) produces the next average structural formula: $(Ca_{0.39}Ce_{0.33}La_{0.13}Nd_{0.12}Pr_{0.04})_{\Sigma 1.01}(Ti_{1.82}Nb_{0.07}Fe^{3+}_{0.02}Zr_{0.02})_{\Sigma 1.93}(O,OH)_6$ (Table 1). Y, Er, Dy and Pb contents in aeschynite-(Ce) have been analysed but they are below detection limit. Therefore, the aeschynite-group minerals from SK-2 kimberlite are poor in Nb, U and Th when compared to similar minerals typically occurring as metamictic phases in carbonatites [37] and metasomatised rocks [38]. However, their compositions are similar to those of the late Ti-REE minerals described in the Iron Mountain kimberlite field [13].

Ti-rich hydrogarnets from the SK-2 kimberlite were analysed by EMPA, while those from the SK-1 pipe are too small to be analysed (Table 2). According to the IMA nomenclature for garnet group minerals [39], schorlomite end member has 2 apfu Ti in Y position, while andradite end member has 2 apfu Fe^{3+} in Y position. The Ti-rich garnets (12.9 wt %–26.3 wt % TiO_2) studied in the present work could correspond to a theoretical hydrous andradite (when it has <1 apfu Ti) and hydrous schorlomite (when it has >1 apfu). However, Ti-rich hydroandradite from the SK-2 kimberlite returns low total (88 wt %–96 wt %) and Si is also very low (1.6–1.9 apfu), thus suggesting the substitution of Si by OH in Z position and the existence of H_2O molecules. They plot inside the field of Ti andradites from ultramafic lamprophyres [25] (Figure 6).

Table 2. Representative EMPA analysis of Ti-rich garnet from SK-2 kimberlites.

(wt %)	#1	#2	#4	#5	#15	#17	#19	#20	#21
SiO ₂	20.20	25.44	21.62	21.86	21.51	23.18	20.69	21.24	20.00
Al ₂ O ₃	0.63	0.69	0.98	0.98	0.85	0.89	0.85	0.84	0.92
Cr ₂ O ₃	0.32	0.83	1.23	0.77	2.81	0.37	2.63	1.25	2.22
TiO ₂	26.33	23.39	14.80	14.60	15.50	13.30	15.64	14.46	16.02
MgO	0.80	1.46	0.08	0.20	0.17	0.47	0.14	0.10	0.68
Na ₂ O	bdl	0.04	bdl	bdl	bdl	bdl	bdl	bdl	bdl
BaO	0.10	0.11	bdl	bdl	bdl	bdl	bdl	0.10	0.11
MnO	0.13	0.09	0.07	0.09	0.06	0.08	0.10	0.08	0.22
FeO	13.62	11.88	14.34	15.16	13.07	16.04	12.42	15.13	14.95
SrO	bdl	bdl	bdl	bdl	bdl	bdl	bdl	bdl	bdl
ZrO ₂	0.79	0.77	0.20	0.28	0.18	0.30	0.54	0.40	0.35
K ₂ O	0.01	0.01	0.02	0.01	0.01	0.01	0.01	bdl	bdl
CaO	30.61	30.24	34.92	34.82	35.19	34.12	35.24	34.94	32.91
Total	93.86	95.22	88.26	88.77	89.35	88.77	88.25	88.53	88.39
Recalculated Analyses									
Fe ₂ O ₃	15.14	13.20	15.94	16.85	14.52	17.83	13.80	16.81	16.61
FeO	0.00	0.00	0.00	0.00	0.00	0.00	0.00	0.00	0.00
Total	95.12	96.28	89.88	90.47	90.81	90.55	89.66	90.26	90.06
(apfu)	Cation for 3(Ca + K + Na + Sr + Ba + Mn + Mg)								
Si	1.7730	2.1941	1.7241	1.7392	1.6971	1.8626	1.6309	1.6883	1.6432
Al	0.0655	0.0704	0.0921	0.0920	0.0793	0.0842	0.0786	0.0788	0.0895
Cr	0.0222	0.0563	0.0778	0.0485	0.1753	0.0238	0.1639	0.0784	0.1442
Ti	1.7385	1.5175	0.8878	0.8738	0.9199	0.8039	0.9273	0.8646	0.9901
Mg	0.1049	0.1878	0.0097	0.0240	0.0201	0.0562	0.0159	0.0119	0.0838
Na	0.0000	0.0063	0.0000	0.0000	0.0000	0.0000	0.0000	0.0000	0.0000
Ba	0.0035	0.0037	0.0000	0.0000	0.0000	0.0000	0.0000	0.0030	0.0036
Mn	0.0097	0.0063	0.0048	0.0060	0.0042	0.0057	0.0066	0.0052	0.0151
Fe ³⁺	0.9996	0.8567	0.9562	1.0085	0.8622	1.0777	0.8186	1.0056	1.0271
Sr	0.0000	0.0000	0.0000	0.0000	0.0000	0.0000	0.0000	0.0000	0.0000
Zr	0.0340	0.0325	0.0077	0.0109	0.0068	0.0118	0.0208	0.0156	0.0141
K	0.0011	0.0013	0.0015	0.0010	0.0009	0.0008	0.0009	0.0000	0.0000
Ca	2.8784	2.7942	2.9833	2.9679	2.9744	2.9373	2.9759	2.9754	2.8968

“bdl”: below detection limit.

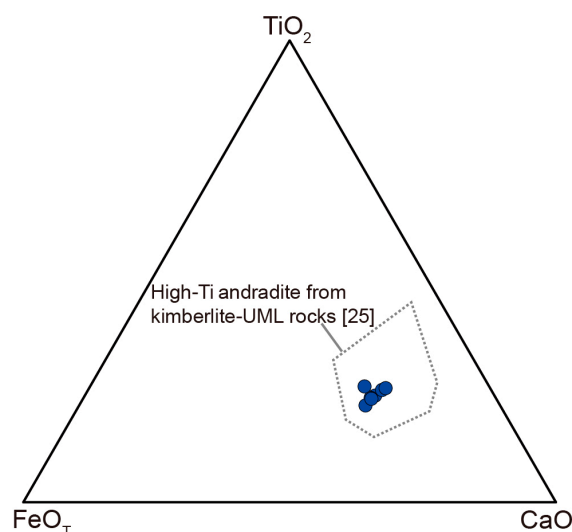


Figure 6. Compositional variation of TiO₂, FeO_T and CaO for Ti-rich garnet from SK-2 kimberlite pipe compared with Ti-rich andradites from ultramafic lamprophyres [25].

5. Discussion

Perovskite is a valuable mineral recorder of the crystallization conditions of the kimberlites. It commonly crystallizes directly from the kimberlite magma [40]. Therefore, pristine primary perovskite grains in both kimberlites and carbonatites are often used for geochemical investigations and, in particular for U-Pb dating [5,6,10,12,13,16–21,41,42]. However, it has been proved that different perovskite generations can occur in the same kimberlite. Simultaneous occurrence of two populations of primary perovskite has been explained by magma mingling [5]. In addition, primary magmatic perovskite can be altered [12,13] during subsolidus processes to secondary minerals that may redistribute REE and potentially, U, Pb and Th [43]. Our petrographic data shows that two types of texturally fresh (i.e., pristine) perovskite occur in the studied Indian kimberlites. Groundmass type 1 crystals may be interpreted as primary magmatic perovskite. However, type 2 perovskite occurs along with calcite and serpentine filling porosity produced by replacement of Ti-rich spinels. This assemblage suggests that type 2 perovskite could be produced by subsolidus hydrothermal phenomena and thus not necessarily related to the primary perovskite. Similar pristine secondary hydrothermal perovskites have been described in carbonatites and cannot be used to obtain the age of the intrusive [23]. Therefore, our observations further restrict the use of groundmass perovskite for geochronological purposes, since they show for the first time that pristine perovskite can be also formed in kimberlites by hydrothermal processes. Therefore, an accurate petrographic study is necessary to exclude perovskite affected by subsolidus processes. Hence, we suggest taking additional cautions when using perovskite grains in concentrates.

The alteration of perovskite is strongly dependent upon pH, $f(\text{CO}_2)$ and temperature. It is expected to occur in late-stage hydrothermal alteration processes and in the subaerial weathering environment [9]. The replacement of perovskite occurs at the late stage of groundmass formation, resulting from a decrease in $f(\text{O}_2)$ and temperature (<350 °C) at low pressure ($P < 2$ kbars) and over a wide range of $a(\text{Mg}^{2+})$ values [12]. The replacement of olivine by serpentine as well as the replacements of perovskite and spinel suggest that $P(\text{CO}_2)$ and $P(\text{H}_2\text{O})$ remained relatively high [13]. The two Indian kimberlites studied here have significant differences regarding their subsolidus history, mainly represented by the higher complexity of perovskite alteration in SK-2. The alteration process took place under different fluid/rock ratios in each kimberlite, in a relatively closed system. Under these conditions, Ti-rich minerals are unstable and, in particular, Ti-rich spinels are easily replaced in both kimberlites by mixtures of Ti-rich hydrogarnets, calcite and serpentine. A relatively low SiO_2 and high water activities were necessary to avoid the crystallization of titanite and to favour the crystallization of hydrogarnets. Slight replacement of perovskite by anatase in SK-1 could be indicative of a decrease of temperature under conditions of medium to high $f(\text{CO}_2)$, following the thermodynamic calculations data [15]. However, the same experimental data suggest that the strong replacement of perovskite by kassite in SK-2 needs a high $f(\text{H}_2\text{O})$ and a low activity in alkalis. The formation of kassite or anatase during perovskite replacement may also involve different rates of Ca-leaching, as kassite formation is favoured by lower Ca-leaching [13]. The LREE-rich perovskite is more unstable during these processes than pure end-member perovskite. Therefore, aeschynite-(Ce) inherits the composition of the replaced LREE-bearing perovskite cores and it is Nb-poor because the cores were also Nb-poor.

The occurrence of abundant Ti-rich garnets in the groundmass of the rock could suggest an aillikitic affinity during a preliminary examination, based on the International Union of Geological Sciences (IUGS) rock classification [44]. Ti-rich garnets in groundmass from Indian kimberlites have been used to classify the rocks as orangeites [25]. Those Ti-rich garnets have similar composition to the Ti-rich garnets studied in the current work, which also plot inside the field of high Ti-andradite from kimberlite-UML rocks (Figure 6). However, hydrogarnets from SK-1 and SK-2 kimberlites replace Ti-rich oxides and are accompanied by hydrothermal minerals such as serpentine and type 2 perovskite, thus indicating that they were produced by late hydrothermal processes. Therefore, these garnets cannot be representative of the parental magma composition. In fact, Ti-rich hydrogarnets have also been found in ophiolite sequences as a result of hydrothermal alteration [33]. Hence, attention must be

paid to the position of Ca-Ti-rich garnet in the mineral sequence before using it to classify the rock based on its occurrence.

6. Conclusions

Two types of perovskite occur in the SK-1 and SK-2 Indian kimberlites. The first type crystallized directly from the kimberlite magma, whereas a hydrothermal origin was inferred from the second. Additionally, two different replacement trends of groundmass perovskite have been identified. Type 1 groundmass perovskite is replaced by anatase in SK-1 and by kassite along with aeschynite-(Ce) in SK-2. The different sequences are related to alteration under different $f(\text{CO}_2)$ and $f(\text{H}_2\text{O})$ conditions. In some cases, perovskite may be strongly altered to secondary minerals, resulting in a redistribution of REE and potentially, U, Pb and Th. Therefore, U-Pb dating studies involving perovskite require a detailed petrographic characterisation to confirm its primary (i.e., magmatic) origin.

Ti-rich hydrogarnets in SK-1 and SK-2 replace groundmass atoll spinel and could correspond to “hydroandradite” and “hydroschorlomite.” They were produced by hydrothermal processes. Therefore, attention must be paid to the position of Ca-Ti-garnet in the mineral sequence and to its water content before using it to classify the rock based on its occurrence.

Acknowledgments: This research was supported by the CGL2006-12973 and CGL2009-13758 projects of the Ministerio de Ciencia e Innovación of Spain, the AGAUR 2014SGR01661 project of the Generalitat de Catalunya and by a FI grant to Jingyao Xu (coded FI_B 00904) sponsored by the Secretaria d’Universitats i Recerca del Departament d’Economia i Coneixement de la Generalitat de Catalunya. The authors also acknowledge the thin section preparation laboratory and the Scientific and Technological Centers of the University of Barcelona (CCiTUB) for the assistance with SEM-BSE-EDS study (Javier García-Veigas, David Artiaga) and EMP analyses (Xavier Llovet). The authors are also very grateful to the two anonymous reviewers for their critical comments.

Author Contributions: Jingyao Xu analysed the data; Joan Carles Melgarejo devised the project and guided analysis and interpretation; Montgarri Castillo-Oliver contributed samples. Jingyao Xu also wrote the paper, assisted by Joan Carles Melgarejo and Montgarri Castillo-Oliver.

Conflicts of Interest: The authors declare no conflict of interest.

References

1. Rezvukhin, D.I.; Malkovets, V.G.; Sharygin, I.S.; Kuzmin, D.V.; Litasov, K.D.; Gibsher, A.A.; Pokhilenko, N.P.; Sobolev, N.V. Inclusions of Cr- and Cr-Nb-Rutile in pyropes from the Internatsionalnaya kimberlite pipe, Yakutia. *Dokl. Earth Sci.* **2016**, *466*, 173–176. [[CrossRef](#)]
2. Ragozin, A.L.; Zedgenizov, D.A.; Shatskii, V.S.; Orihashi, Y.; Agashev, A.M.; Kagi, H. U-Pb age of rutile from the eclogite xenolith of the Udachnaya kimberlite pipe. *Dokl. Earth Sci.* **2014**, *457*, 861–864. [[CrossRef](#)]
3. Roeder, P.L.; Schulze, D.J. Crystallization of groundmass spinel in kimberlite. *J. Petrol.* **2008**, *49*, 1473–1495. [[CrossRef](#)]
4. Bellis, A.; Canil, D. Ferric Iron in CaTiO_3 perovskite as an oxygen barometer for kimberlitic magmas I: Experimental calibration. *J. Petrol.* **2007**, *48*, 219–230. [[CrossRef](#)]
5. Castillo-Oliver, M.; Galí, S.; Melgarejo, J.C.; Griffin, W.L.; Belousova, E.; Pearson, N.J.; Watangua, M.; O’Reilly, S.Y. Trace-element geochemistry and U-Pb dating of perovskite in kimberlites of the Lunda Norte province (NE Angola): Petrogenetic and tectonic implications. *Chem. Geol.* **2016**, *426*, 118–134. [[CrossRef](#)]
6. Batumike, J.M.; Griffin, W.L.; Belousova, E.A.; Pearson, N.J.; O’Reilly, S.Y.; Shee, S.R. LAM-ICPMS U-Pb dating of kimberlitic perovskite: Eocene-Oligocene kimberlites from the Kundelungu Plateau, D.R. Congo. *Earth Planet. Sci. Lett.* **2008**, *267*, 609–619. [[CrossRef](#)]
7. Tappe, S.; Kjarsgaard, B.A.; Kurszlaukis, S.; Nowell, G.M.; Phillips, D. Petrology and Nd-Hf Isotope Geochemistry of the Neoproterozoic Amon Kimberlite Sills, Baffin Island (Canada): Evidence for Deep Mantle Magmatic Activity Linked to Supercontinent Cycles. *J. Petrol.* **2014**, *55*, 2003–2042. [[CrossRef](#)]
8. Malkovets, V.G.; Rezvukhin, D.I.; Belousova, E.A.; Griffin, W.L.; Sharygin, I.S.; Tretiakova, I.G.; Gibsher, A.A.; O’Reilly, S.Y.; Kuzmin, D.V.; Litasov, K.D.; et al. Cr-rich rutile: A powerful tool for diamond exploration. *Lithos* **2016**, *265*, 304–311. [[CrossRef](#)]
9. Mitchell, R.H. *Perovskites Modern and Ancient*; Almaz Press: Thunder Bay, ON, Canada, 2002.

10. Chakhmouradian, A.R.; Mitchell, R.H. Three compositional varieties of perovskite from kimberlites of the Lac de Gras field (Northwest Territories, Canada). *Mineral. Mag.* **2001**, *65*, 133–148. [[CrossRef](#)]
11. Chalapathi Rao, N.V.; Lehmann, B.; Mainkar, D.; Belyatsky, B. Petrogenesis of the end-Cretaceous diamondiferous Behradih orangeite pipe: Implication for mantle plume-lithosphere interaction in the Bastar craton, Central India. *Contrib. Mineral. Petrol.* **2011**, *161*, 721–742. [[CrossRef](#)]
12. Chakhmouradian, A.R.; Mitchell, R.H. Occurrence, alteration patterns and compositional variation of perovskite in kimberlites. *Can. Mineral.* **2000**, *38*, 975–994. [[CrossRef](#)]
13. Mitchell, R.H.; Chakhmouradian, A.R. Instability of perovskite in a CO₂-rich environment: Examples from carbonatite and kimberlite. *Can. Mineral.* **1998**, *36*, 939–952.
14. Pereira, V.P.; Conceicao, R.V.; Formoso, M.L.L.; Pires, A.C. Alteration of perovskite to anatase in silica-undersaturated rocks of the Catalao I carbonatite complex, Brazil; a Raman study. *Rev. Bras. Geociênc.* **2005**, *35*, 239–244.
15. Martins, T.; Chakhmouradian, A.R.; Medici, L. Perovskite alteration in kimberlites and carbonatites: The role of kassite, CaTi₂O₄(OH)₂. *Phys. Chem. Miner.* **2014**, *41*, 473–484. [[CrossRef](#)]
16. Heaman, L.M.; Kjarsgaard, B.A. Timing of eastern North American kimberlite magmatism: Continental extension of the Great Meteor hotspot track? *Earth Planet. Sci. Lett.* **2000**, *178*, 253–268. [[CrossRef](#)]
17. Chalapathi Rao, N.V.; Wu, F.Y.; Mitchell, R.H.; Li, Q.L.; Lehmann, B. Mesoproterozoic U-Pb ages, trace element and Sr-Nd isotopic composition of perovskite from kimberlites of the Eastern Dharwar craton, southern India: Distinct mantle sources and a widespread 1.1Ga tectonomagmatic event. *Chem. Geol.* **2013**, *353*, 48–64. [[CrossRef](#)]
18. Heaman, L.M.; Kjarsgaard, B.A.; Creaser, R.A. The temporal evolution of North American kimberlites. *Lithos* **2004**, *76*, 377–397. [[CrossRef](#)]
19. Paton, C.; Hergt, J.M.; Phillips, D.; Woodhead, J.D.; Shee, S.R. New insights into the genesis of Indian kimberlites from the Dharwar Craton via in situ Sr isotope analysis of groundmass perovskite. *Geology* **2007**, *35*, 1011–1014. [[CrossRef](#)]
20. Woodhead, J.; Hergt, J.; Phillips, D.; Paton, C. African kimberlites revisited: In situ Sr-isotope analysis of groundmass perovskite. *Lithos* **2009**, *112*, 311–317. [[CrossRef](#)]
21. Zurevinski, S.E.; Heaman, L.M.; Creaser, R.A. The origin of Triassic/Jurassic kimberlite magmatism, Canada: Two mantle sources revealed from the Sr-Nd isotopic composition of groundmass perovskite. *Geochem. Geophys. Geosyst.* **2011**, *12*. [[CrossRef](#)]
22. Kukhareno, A.A.; Orlova, M.P.; Bulakh, A.G.; Bagdasarov, E.A.; Rimski-Korsakov, O.M.; Nefedov, E.I.; Ilyinskiy, G.A.; Sergeev, A.B.; Abakumova, N.B. *The Caledonian Ultramafic Alkaline and Carbonatite Complexes of the Kola Peninsula and Northern Karelia*; Nedra: Moscow, Russia, 1965.
23. Lepekhina, E.N.; Antonov, A.V.; Savva, E.V.; Belyatsky, B.V.; Sergeev, S.A. Perovskite from the Tikshezzero carbonatite: Age and genesis. In *Perovskite from the Tikshezzero Carbonatite: Age and Genesis. Extended Abstract: Geochemistry of Magmatic Rocks—School Geochemistry of Alkaline Rocks*; Vernadsky Institute of Geochemistry and Analytical Chemistry, Russian Academy of Sciences: Moscow, Russia, 2009.
24. Tappe, S.; Jenner, G.A.; Foley, S.F.; Heaman, L.; Besserer, D.; Kjarsgaard, B.A.; Ryan, B. Torngat ultramafic lamprophyres and their relation to the North Atlantic Alkaline Province. *Lithos* **2004**, *76*, 491–518. [[CrossRef](#)]
25. Dongre, A.N.; Viljoen, K.S.; Chalapathi Rao, N.V.; Guzik, A. Origin of Ti-rich garnets in the groundmass of Wajrakarur field kimberlites, southern India: Insights from EPMA and Raman spectroscopy. *Mineral. Petrol.* **2016**, *110*, 295–307. [[CrossRef](#)]
26. Tappe, S.; Foley, S.F.; Jenner, G.A.; Heaman, L.M.; Kjarsgaard, B.A.; Romer, R.L.; Stracke, A.; Joyce, N.; Hoefs, J. Genesis of ultramafic lamprophyres and carbonatites at Aillik Bay, Labrador: A consequence of incipient lithospheric thinning beneath the North Atlantic Craton. *J. Petrol.* **2006**, *47*, 1261–1315. [[CrossRef](#)]
27. Hammond, A.L.; Mitchell, R.H. Accessory mineralogy of orangeite from Swartruggens, South Africa. *Mineral. Petrol.* **2002**, *76*, 1–19. [[CrossRef](#)]
28. Müntener, O.; Hermann, J. Titanian andradite in a metapyroxenite layer from the Malenco ultramafics (Italy): Implications for Ti-mobility and low oxygen fugacity. *Contrib. Mineral. Petrol.* **1994**, *116*, 156–168. [[CrossRef](#)]
29. Amthauer, G.; Rossman, G.R. The hydrous component in andradite garnet. *Am. Mineral.* **1998**, *83*, 835–840. [[CrossRef](#)]

30. Laverne, C.; Grauby, O.; Alt, J.C.; Bohn, M. Hydroschorlomite in altered basalts from Hole 1256D, ODP Leg 206: The transition from low-temperature to hydrothermal alteration. *Geochem. Geophys. Geosyst.* **2006**, *7*. [[CrossRef](#)]
31. Schingaro, E.; Lacalamita, M.; Mesto, E.; Ventruti, G.; Pedrazzi, G.; Ottolini, L.; Scordari, F. Crystal chemistry and light elements analysis of Ti-rich garnets. *Am. Mineral.* **2016**, *101*, 371–384. [[CrossRef](#)]
32. Dongre, A.N.; Jacob, D.E.; Stern, R.A. Subduction-related origin of eclogite xenoliths from the Wajrakarur kimberlite field, Eastern Dharwar craton, Southern India: Constraints from petrology and geochemistry. *Geochim. Cosmochim. Acta* **2015**, *166*, 165–188. [[CrossRef](#)]
33. Ghosh, B.; Morishita, T.; Ray, J.; Tamura, A.; Mizukami, T.; Soda, Y.; Oving, T.N. A new occurrence of titanian (hydro)andradite from the Nagaland ophiolite, India: Implications for element mobility in hydrothermal environments. *Chem. Geol.* **2017**, *457*, 47–60. [[CrossRef](#)]
34. Downs, R.T. The RRUFF Project: An integrated study of the chemistry, crystallography, Raman and infrared spectroscopy of minerals. In *Program and Abstracts of the 19th General Meeting of the International Mineralogical Association*; International Mineralogical Association: Kobe, Japan, 2006; pp. O03–O13.
35. Paschoal, C.W.A.; Moreira, R.L.; Fantini, C.; Pimenta, M.A.; Surendran, K.P.; Sebastian, M.T. Raman scattering study of RETiTaO6 dielectric ceramics. *J. Eur. Ceram. Soc.* **2003**, *23*, 2661–2666. [[CrossRef](#)]
36. Tomašić, N.; Gajović, A.; Bermanec, V.; Rajić, M. Recrystallization of metamict Nb–Ta–Ti–REE complex oxides: A coupled X-Ray-Diffraction and Raman Spectroscopy study of aeschynite-(Y) and polycrase-(Y). *Can. Mineral.* **2004**, *42*, 1847–1857. [[CrossRef](#)]
37. Nasir, S.; Theye, T.; Massonne, H.J. REE-Rich Aeschynite in Apatite-Dolomite Carbonatite, Eastern Oman Mountains. *Open Mineral. J.* **2009**, *3*, 17–27.
38. Macdonald, R.; Bagiński, B.; Kartashov, P.M.; Zozulya, D.; Dzierżnowski, P. Hydrothermal alteration of chevkinite-group minerals. Part 2. Metasomatite from the Keivy massif, Kola Peninsula, Russia. *Mineral. Mag.* **2015**, *79*, 1039–1059. [[CrossRef](#)]
39. Grew, E.S.; Locock, A.J.; Mills, S.J.; Galuskina, I.O.; Galuskin, E.V.; Hålenius, U. IMA report: Nomenclature of the garnet supergroup. *Am. Mineral.* **2013**, *98*, 785–810. [[CrossRef](#)]
40. Mitchell, R.H. *Kimberlites: Mineralogy, Geochemistry, and Petrology*; Plenum Press: New York, NY, USA, 1986.
41. Cox, R.A.; Wilton, D.H.C. U–Pb dating of perovskite by LA-ICP-MS: An example from the Oka carbonatite, Quebec, Canada. *Chem. Geol.* **2006**, *235*, 21–32. [[CrossRef](#)]
42. Simonetti, A.; Heaman, L.M.; Chacko, T. Use of discrete-dynode secondary electron multipliers with Faradays—A “reduced volume” approach for in-situ U–Pb dating of accessory minerals within petrographic thin sections by LA-MC-ICP-MS. In *Laser Ablation-ICP-MS in the Earth Sciences*; Short Course Series 40; Ylvester, P., Ed.; Mineralogical Association of Canada: Quebec, QC, Canada, 2008; pp. 24–264.
43. Yang, Y.H.; Wu, F.Y.; Wilde, S.A.; Liu, X.M.; Zhang, Y.B.; Xie, L.W.; Yang, J.H. In situ perovskite Sr–Nd isotopic constraints on the petrogenesis of the Ordovician Mengyin kimberlites in the North China Craton. *Chem. Geol.* **2009**, *264*, 24–42. [[CrossRef](#)]
44. Tappe, S.; Foley, S.F.; Jenner, G.A.; Kjarsgaard, B.A. Integrating ultramafic lamprophyres into the IUGS classification of igneous rocks: Rationale and implications. *J. Petrol.* **2005**, *46*, 1893–1900. [[CrossRef](#)]

